Chapter 16
Is Silicon Photonics a Competitive Technology to Enable Better and Highly Performing Networks?

Kensuke Ogawa and Kenji Nishide

Abstract This chapter focuses on the fundamental and high-speed characteristics of small-footprint integrated optical modulators designed and fabricated on the basis of the silicon-photonic platform to assess their key performance factors in applications related to high-capacity energy-efficient optical networks transmitting data in various modulation formats. The design and characteristics of high-speed silicon rib-waveguide phase shifters, which are most essential in the high-speed optical modulators, are described. A low-loss quasi-single-mode silicon rib-waveguide phase shifter with reduced RC delay is highlighted along with its design features and fundamental performances in terms of optical loss and on/off dynamic response. Free-carrier plasma dispersion is reviewed as a physical process for performing optical modulation, which allows a reduction in thermal drift and frequency chirping. The plasma dispersion has a unique property in that signal distortion due to residual intensity modulation cancels with the nonlinear voltage dependence of the optical phase, thereby being useful for zero-chirp optical modulators to eliminate transmission impairments. The on-off keying performance of a silicon optical modulator using a single Mach–Zehnder interferometer waveguide is described in the first example of optical network applications with emphasis on a 10-Gb/s dispersion tolerance comparable to that of a commercial lithium niobate modulator. The advantage of silicon-photonic integration is remarkable, in particular, for the ultrasmall-footprint silicon optical modulator consisting of a pair of IQ nested Mach–Zehnder interferometers for two orthogonal polarization components and a polarization multiplexer monolithically integrated on a silicon chip. Such a chip is presented with respect to applications in digital coherent communication in optical-fiber links up to 1000 km long at a bit rate as high as 128 Gb/s.

K. Ogawa (✉) · K. Nishide
Advanced Technology Laboratory, Fujikura Ltd,
1440 Mutsuzaki, Sakura, Chiba 285-8550, Japan
e-mail: kensuke.ogawa@jp.fujikura.com

K. Nishide
e-mail: kenji.nishide@jp.fujikura.com

16.1 Introduction

High-speed photonic components such as optical modulators operating at bit rates of 10 Gb/s or beyond play significant roles in efficient data transmission in modern optical systems and subsystems. They have been extensively deployed in long-haul optical-fiber telecommunications, and now are adapted to metro-area networks, datacoms, RF photonic links, and on-chip/on-board optical interconnects [1–9]. Photonic integration allows small-footprint high-efficiency photonic components to realize compact and energy-efficient systems and subsystems for high-speed optical data transmission.

There have been arguments in terms of the *pros and cons* of silicon photonics from the point of view of platform technology for monolithic and heterogeneous integration of photonic device blocks to build highly functional photonic integrated circuits (PICs) with both performances and manufacturing costs matching the requirements of the market in the field of high-speed optical networks [10, 11]. High-density integration based on high-index-contrast waveguide optics and low-cost fabrication using CMOS-based processes are favored for high-speed optical transceivers in small footprints, optical switches of high port counts, and so on. It has been often pointed out, however, that the optical and optoelectronic performances of silicon-based PICs do not parallel those of the competing counterpart devices made of electro-optic insulators or compound semiconductors, such as lithium niobate and indium phosphide, and thus provide limited capabilities of application in compensation for the potential benefits of integration and cost reduction.

To obtain an insight into the issue raised above, this chapter focuses on the fundamentals and high-speed characteristics of small-footprint integrated optical modulators designed and fabricated on the basis of the silicon-photonic platform to assess their key performance factors for applications in high-capacity energy-efficient optical networks transmitting data in various modulation formats. The optical modulators reviewed in this chapter are Mach–Zehnder (MZ) modulators because of their advantages of high-contrast modulation in the broad spectral ranges of the C and L bands [12] and chirp-free modulation under push-pull drive [4, 13, 14].

The chapter is organized as follows:

- In Sect. 16.2, the design and characteristics of silicon rib-waveguide phase shifters are described. Reverse-biased lateral PN-junction quasi-single-mode rib-waveguide phase shifters are the most essential parts of the high-speed optical modulators to achieve high-speed optical phase modulation with low optical loss [15]. The key points and efforts for reduction in optical loss and *RC* delay are described.
- In Sect. 16.3, free-carrier plasma dispersion, which is the physical process generating refractive-index modulation [16], is reviewed in the light of high-performance optical phase modulation. The broadband spectral response of free-carrier plasma dispersion, which is crucial to the suppression of thermal

drift and the wavelength dependence of optical phase modulation, is clarified based on the Drude model of conducting carriers in solids in contrast with compound semiconductor optical phase modulator based on quantum-well electroabsorption [17]. It is also shown that free-carrier plasma dispersion is suitable for the suppression of frequency chirping without transmission impairment, thereby endowing a zero-chirp optical modulator with a unique property that the signal distortion due to residual intensity modulation cancels with the nonlinear voltage dependence of optical phase.

- In Sect. 16.4, performances of zero-chirp silicon optical modulators are assessed in applications to data transmission using on-off keying (OOK), binary phase-shift keying (BPSK), quadrature phase-shift keying (QPSK) and dual-polarization quadrature phase-shift keying (DP-QPSK) modulation formats. The last modulation format is exploited for digital coherent communication in high-capacity high-spectral-efficiency optical transport networks at bit rates of 100 Gb/s and higher [18–21]. On-off keying performances of a silicon optical modulator using a single MZ interferometer waveguide at 10-Gb/s bit rate are described in the first example of optical network applications with emphasis on a dispersion tolerance comparable with that of a commercialized lithium niobate (LN) modulator. The advantage of silicon-photonic integration is remarkable, in particular, for the ultrasmall-footprint silicon optical modulator consisting of a pair of IQ nested MZ interferometers for two orthogonal polarization components and a polarization multiplexer integrated monolithically on a silicon chip, which is presented with respect to applications in digital coherent communication in optical-fiber links at distances up to 1000 km and at bit rates as high as 128 Gb/s.

16.2   Fundamental Characteristics of Rib-Waveguide Phase Shifter

16.2.1   Rib-Waveguide Phase Shifter in MZ Interferometer

The rib-waveguide phase shifter inserted in each arm of a MZ interferometer (MZI), as shown in Fig. 16.1, is most essential for high-speed modulation. The optical modulators including MZIs were fabricated on 200-mm diameter silicon-on-insulator (SOI) wafers by using 130-nm node CMOS fabrication processes [22]. The core of the rib waveguide is made of crystalline silicon of the SOI layer. The core is surrounded by top and bottom silicon-dioxide clads. A buried oxide (BOX) layer of the SOI wafer is used as the bottom clad. Silicon rectangular waveguides were used for the other parts of the MZI. The transverse-electric polarization (TE) is stable in the rib waveguide.

A depletion region is located at the boundary of the lateral PN junction in the middle of the rib core under application of a DC reverse bias to the junction. The horizontal width of the depletion region is controlled and thereby the effective
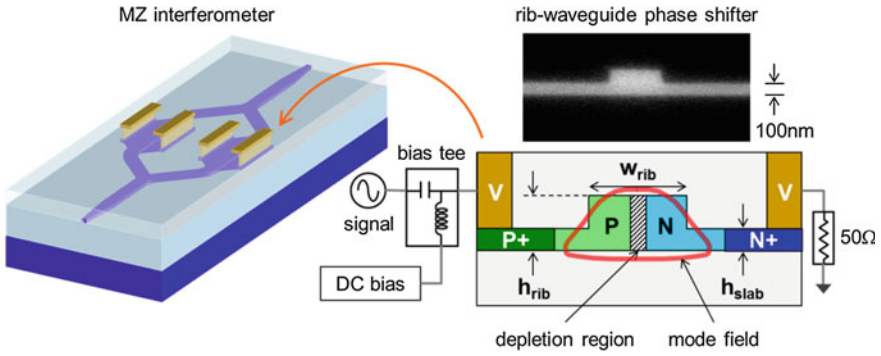
Fig. 16.1 Illustration and SEM image of cross section of rib-waveguide phase shifter inserted in each arm of MZ interferometer with the electrical connection schematic for DC bias and high-speed signal to the PN-junction of the phase shifter via vertical metal interconnect (V)
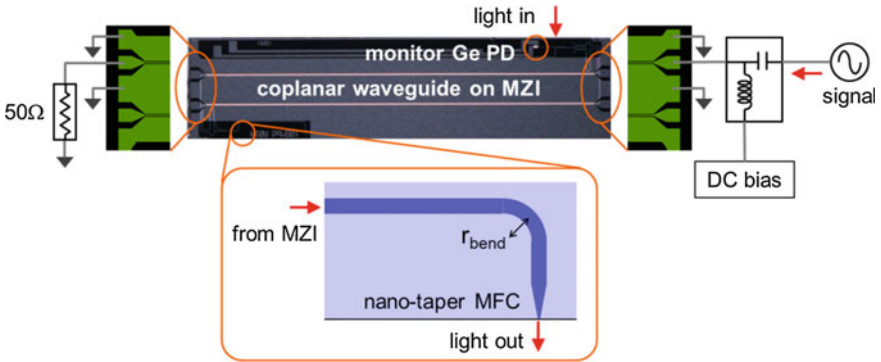

Fig. 16.2 *Top-view* image of an integrated silicon single MZI modulator chip with a schematic diagram of the electrical connection to contact pads on coplanar waveguide electrodes and an illustrated layout of the output waveguide end

refractive index of the rib waveguide is controlled with a signal voltage applied to the PN junction in conjunction with the DC reverse bias [23]. High-speed refractive-index modulation is induced by the high-speed drift motion of electrons and holes near the depletion region under the reverse bias [24].

High-speed electrical signals carrying data are input to a contact pad of a signal line electrode of a coplanar waveguide, which is connected to a rib-waveguide phase shifter in one arm of a silicon MZI through a bias tee, as shown in Fig. 16.2. The DC reverse bias to each phase shifter can be adjusted for optimum modulation performance. The coplanar waveguide was designed using short and straight signal electrodes without bending to eliminate RF signal distortion, thereby enhancing the electro-optic (EO) response beyond 33 GHz [12, 25].

Optical-fiber coupling using straight silicon waveguides connected to both ends of the silicon MZI is not allowed due to a clash with the RF bonding wires connected to the contact pads on the coplanar waveguide electrodes. To avoid this issue, input and output ends of the waveguides were placed on the side facets using high-index-contrast Si channel waveguide bends of 25-µm bending radius (r_{bend}), as shown in Fig. 16.2. The optical loss of the waveguide bends is as low as 0.04 dB per semicircle, and therefore negligible [12, 25]. The low-loss optical beam bending was integrated with the silicon MZI in a footprint as small as 5×1 mm^2 using the silicon-photonic platform. Inverted nano-taper mode-field converters (MFCs) were formed for edge coupling to optical fibers with a coupling loss <2.5 dB per facet [25]. A monolithic monitor Ge PD, which was integrated with a high-index-contrast mode splitter waveguide, allows low-loss performance monitoring of the MZ modulator [26].

16.2.2   Optical Loss Characteristics

Reduction in optical loss in the rib-waveguide phase shifter is crucial for the performance of high-speed silicon optical modulators in the light of the increase in optical signal-to-noise ratio (OSNR) for applications to optical transport networks [21]. Optical loss due to light scattering by side-wall roughness is a significant portion of the phase-shifter optical loss. There are two major paths to approach this subject. One is, of course, to utilize the most advanced CMOS fabrication processes capable of producing smooth and flat waveguide side walls with the finest lithographic and dry etching resolutions. Further reduction in the phase-shifter optical loss is achieved by the other approach including the design consideration of the rib-waveguide phase shifters and the optimization of dopant distribution surrounding the PN junction, as described below.

Light scattering at the rib-waveguide side walls becomes less significant if the width of the top part of the rib core, w_{rib}, is increased, because mode overlap with the side walls is weaker for a wider rib top since weaker tails exist at the side walls. Passive optical losses per unit length of silicon rib waveguides with different rib widths without any doping for the PN junction, averaged over 1545–1555 nm in C band and 1595–1605 nm in L band [27], are listed in Tables 16.1 and 16.2, respectively. The optical losses were measured in transverse-electric (TE) polarization, which is the propagation mode more dominant in the rib waveguides than transverse-magnetic (TM) polarization. The rib waveguides were fabricated using an SOI wafer having a 220-nm thick SOI layer with waveguide dimension parameters, $h_{rib} = 220$ nm and $h_{slab} = 95$ nm, respectively.

A rib waveguide with a wider rib core is favorable for the phase shifters in terms of lower passive optical loss. There is another aspect to be considered, however, to realize high-performance optical modulation using the silicon rib-waveguide phase shifters. Higher-order modes exist as guided modes in the rib waveguides if the rib width is wider than 400 nm. The propagation of higher-order guided modes results

Table 16.1 Optical loss of silicon rib waveguides averaged over 1545–1555 nm in C band

Rib width	400 nm	500 nm	600 nm
loss	0.107 dB/mm	0.074 dB/mm	0.057 dB/mm

Table 16.2 Optical loss of silicon rib waveguides averaged over 1595–1605 nm in L band

Rib width	400 nm	500 nm	600 nm
loss	0.084 dB/mm	0.071 dB/mm	0.055 dB/mm

in performance degradation in optical modulation due to reduction in the on/off extinction ratio in intensity modulation or the Q factor in phase modulation. The higher-order mode propagation must be eliminated for high-performance optical modulation. Profiles of absolute electric fields of the fundamental and first higher-order modes are plotted for rib widths of 400–600 nm in Fig. 16.3. The first higher-order mode is not confined in the rib core and radiated out of it. Single-mode propagation is assured for the 400-nm rib waveguide. The first higher-order mode with a rib width wider than 400 nm, on the other hand, is more strongly localized within the central rib area and more stably propagated through the phase shifter waveguide. The mode profiles in TE polarization were obtained by the film-mode-matching method [28].

Optical attenuation is caused by the optical absorption by free electrons and holes introduced in the PN-junction and adjacent areas by a series of P-and N-doping processes. The higher-order modes are attenuated much more significantly than the fundamental mode if highly doped P+ and N+ areas are formed in the side slab parts of the rib waveguides, as illustrated in Fig. 16.1, because the higher-order modes are more extended towards the side slab wings. The concentration of dopants is typically on the order of 10^{17} cm^{-3} for the P and N areas around the central PN junction and on the order of 10^{18} cm^{-3} in the P+ and N+ areas in the side slab parts, respectively. The carrier-induced optical absorption is, therefore, ten times higher in the P+ and N+ areas than in the central PN junction [16]. The fundamental mode is strongly localized in the central rib part and attenuated negligibly due to the high carrier-induced optical absorption in the side slab parts. With the formation of the side P+ and N+ areas, quasi-single-mode propagation is thereby allowed for the rib-waveguides having a rib width wider than 400 nm. In the simulation of the mode fields, h_{rib} and h_{slab} are 220 and 95 nm, respectively, as in the fabricated waveguides. A rib width of about 500 nm is the optimum choice for an on/off extinction ratio as high as 14 dB at a symbol rate of 10 Gbaud with an on-chip phase shifter optical loss as low as 3 dB [15]. Greater reduction in the phase shifter loss is possible by using a wider rib width, but with a reduction in the extinction ratio as the electric field of the first higher-order mode is less extended towards the side wings. One can further optimize the rib width in terms of the extinction ratio and the optical loss with the accumulation of simulation data on the phase shifters.
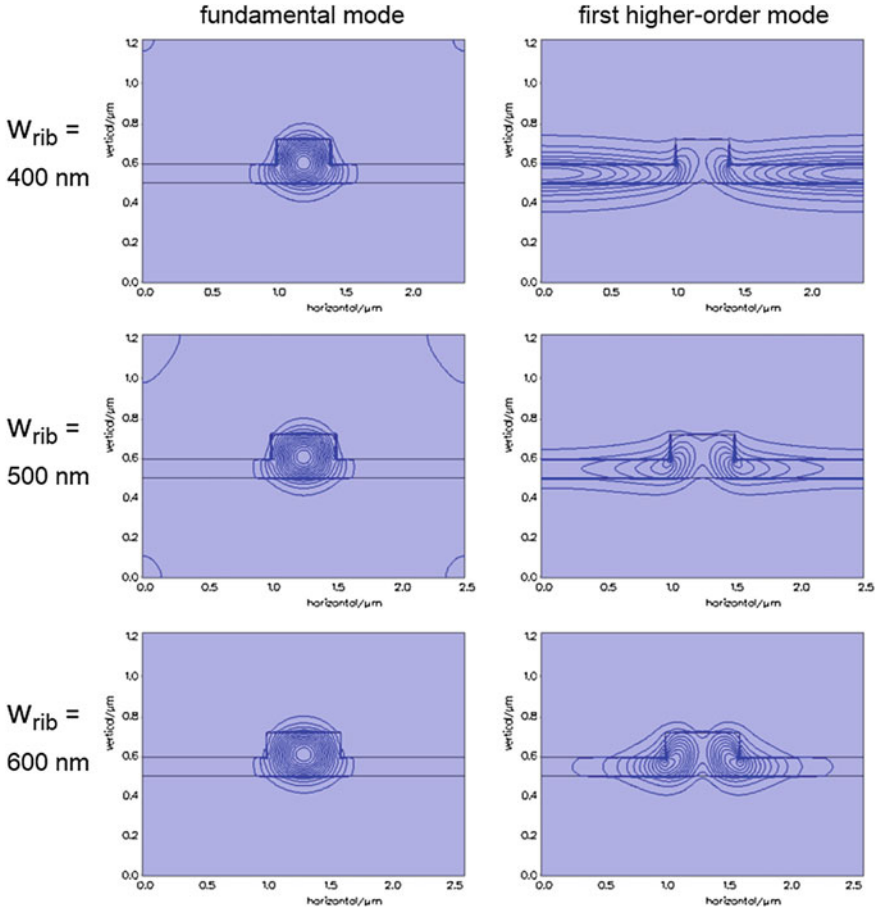
Fig. 16.3 Electric-field contour profiles of fundamental and first higher-order modes in TE polarization in silicon rib waveguides with rib widths of 400, 500, and 600 nm

DC reverse bias dependences of optical phase shift and optical loss were obtained numerically by the simulation of the carrier distribution profile in the PN junction in the silicon rib-waveguide phase shifter with W_{rib} = 500 nm in conjunction with optical-mode-field simulation. The simulation of the two-dimensional electron and hole distribution profile was performed by means of a finite-element solver for the charge continuity and carrier transport equation combined with the Poisson equation. A dopant profile similar to that presented in the literature was adopted [22]. Electron and hole concentrations in N and P areas in the PN junction are 2×10^{17} cm^{-3} and 5×10^{17} cm^{-3}. The carrier distribution profile was converted to a refractive-index profile in the rib waveguide using the empirical formula on the free-carrier plasma dispersion [16, 29]. Higher free-carrier concentration leads to lower refractive index in crystalline Si.
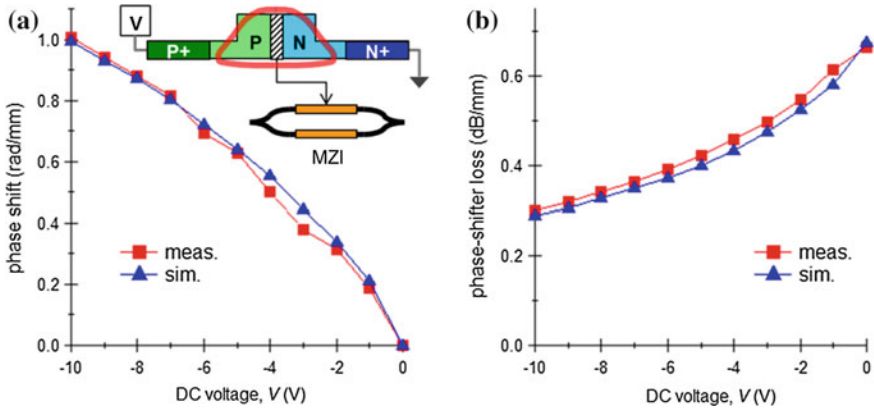
Fig. 16.4 DC reverse bias dependences of the phase shift and optical loss per unit length in a Si rib-waveguide phase shifter

The mode-field simulation using the simulated refractive-index profile in the rib-waveguide phase shifter was based on the beam propagation method [30], which was proven to generate solutions for the mode-field profiles almost the same as those by the film-mode-matching method. The simulated phase shift and carrier-induced optical loss, as plotted in Fig. 16.4, coincide well with the experimental results. This implies that the phase shifter was fabricated with the precise specifications as designed. Further reduction in π-shift voltage, V_π and enhancement of the phase shifter efficiency are possible by design optimization on the doping profile. A voltage-length product defined as $V_\pi \ell$ is a measure of the phase shifter efficiency, obtained as 2.5 V·cm at a reverse bias of –5 V. The residual intensity modulation due to the carrier-induced optical loss is negligible according to the analysis in the literature [14]. The characteristics of the residual intensity modulation are further analyzed with respect to frequency chirping in the next section.

A simultaneous reduction in V_π and the phase-shifter optical loss is not achieved only by adjustment of the doping concentration. Special design improvement is required to overcome this technical difficulty. One of the approaches to this task was adopted by introducing low-doped side-wall areas into the rib-waveguide phase shifters. The low-doped side wall areas, which were formed by compensation doping, namely counter doping to reduce carrier concentration via recombination of carriers of opposite charge polarities, were adopted and proved to be effective for reduction in carrier-induced optical loss without increase in V_π. [31]. The DC performance of a compensation-doped silicon rib-waveguide phase shifter is evaluated in the DC figure of merit (FOM) plotted in Fig. 16.5 as a function of DC reverse bias voltage, V. DC FOM is defined as

$$\text{FOM} = \frac{\pi}{\alpha \ell V_\pi} \qquad (16.1)$$

Fig. 16.5 DC FOM plotted against DC reverse bias voltage for silicon rib-waveguide phase shifters with base-doping only and with compensation doping
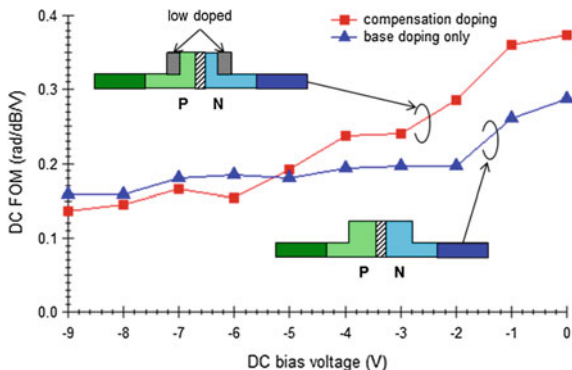
in which α and ℓ are optical loss per unit length and phase shifter length, respectively. At a DC voltage above –2 V, DC FOM is enhanced almost 30 % in the compensation-doped phase shifter in comparison with the phase shifter with base doping only, which is the rib-waveguide phase shifter shown in Fig. 16.1. The DC FOM of the compensation-doped structure is slightly lower than that with base doping only at a DC voltage below –6 V, because the depletion region is extended closer to the side walls. Optical modulation with lower optical loss at a lower RF voltage is allowed with the compensation-doped phase shifter at a total voltage not lower than –6 V. The electro-optic (EO) responses presented in this section and the high-speed modulation performances in various network applications in the next section were acquired with silicon MZI modulators with compensation-doped phase shifters.

16.2.3   Series Resistance Reduction for Shorter RC Delay

In applications to high-capacity optical networks, *RC* delay is one of the major factors limiting the performances of reverse-biased silicon PN-junction phase shifters. Reduction in the series resistance *R* is crucial, in particular, to preserve V_{π} as low as possible, because high capacitance is essential for efficient modulation of the carrier concentration, and hence efficient refractive-index modulation in the PN junction. The slab wings in both sides of the central rib core are a resistance bottleneck and adjustment of the slab height h_{slab} is required to reduce the series resistance in the rib waveguide, as shown in Fig. 16.6.

A remarkable reduction in *RC* delay, thereby shortening the rise and fall times in on/off intensity modulation traces, was confirmed for a silicon single MZI modulator having rib-waveguide phase shifters with $h_{slab} = 95$ nm in comparison with that with $h_{slab} = 60$ nm [17]. The rise and fall times were measured by applying a square-like periodic RF waveform to a phase shifter in one arm of MZI in each modulator. Mean rise and fall times in the input RF waveform are 20.8 and 21.4 ps.
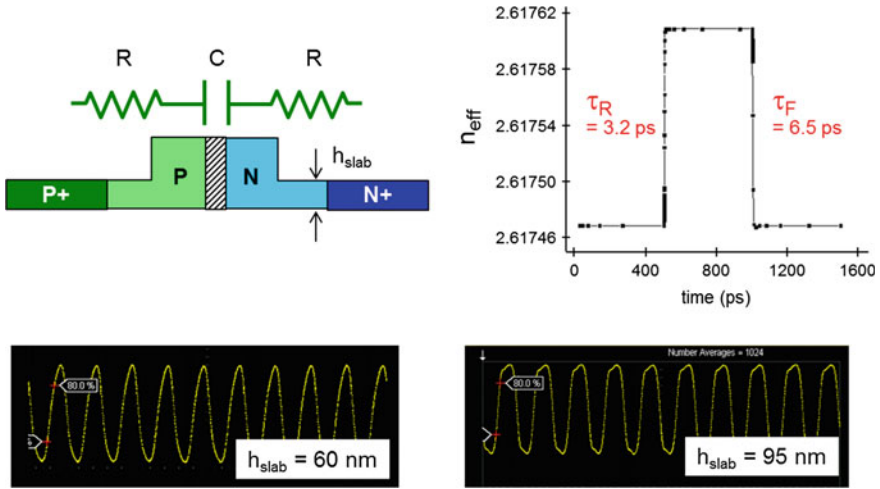
Fig. 16.6 Equivalent circuit model of a silicon rib-waveguide phase shifter, numerical response without series resistance and on/off modulation traces for the phase shifters with h_{slab} = 60 and 95 nm, respectively

In the output waveforms, mean rise and fall times are 39.8 and 29.0 ps for the modulator with h_{slab} = 60 nm, and are 22.2 and 21.5 ps with h_{slab} = 95 nm. The reduction in the rise time is more than 17 ps in good agreement, within the limit of measurement time resolution, with the estimation based on the equivalent circuit model as below. The highly doped side P+ and N+ areas are also advantageous for low series resistances with shorter RC delay. The fall-time reduction is 7.5 ps, limited by the response time of the measurement apparatus consisting of a main frame of sampling oscilloscope and a plug-in unit for optical detection.

The RC delay time for a rib-waveguide PN-junction phase shifter, τ, is represented as

$$\tau = 2RC \tag{16.2}$$

with series resistance in a slab wing in each side, R and capacitance of the PN junction, C [15]. The series resistance R is reduced from 8.2 to 5.7 Ω with h_{slab} increased from 60 to 95 nm. The capacitance C is 1.6 pF for a 4 mm-long phase shifter at DC reverse bias voltage below –2 V [22]. Therefore, τ is estimated as 18 ps in the phase shifter with 95-nm slab wings, while as 26 ps for that with 60-nm slab wings. This leads to a reduction in each of the rise and fall times by 16 ps in the output optical waveforms.

The transient refractive-index response was obtained numerically from the time-dependent solution of the two-dimensional electron and hole distribution profile, as plotted in Fig. 16.6. The series resistance was not incorporated in the device model and the total response time, $\tau_R + \tau_F$ is 9.7 ps. The frequency response of the phase shifter is thus as fast as 100 GHz. Further reduction in the series

Fig. 16.7 EO responses of Si MZI modulators with 3 and 4-mm phase shifters and illustrated configuration for RF signal and DC bias in the S-parameter measurement
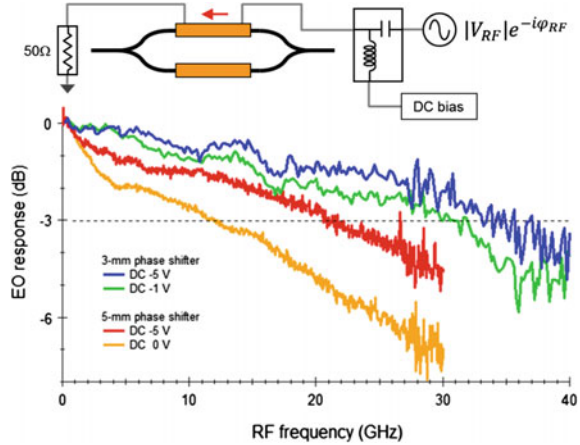
resistance and improvement in the EO response, as described next, will allow optical modulation at symbol rates up to 100 Gbaud and higher with the reverse-biased lateral PN-junction rib-waveguide phase shifter.

16.2.4   EO Response

EO responses of silicon single MZI modulators with 3 and 5-mm phase shifters with W_{rib} = 500 nm obtained in S-parameter measurements are shown in Fig. 16.7 [12, 25]. The RF sinusoidal signal from a vector network analyzer was fed through a bias tee with a DC reverse bias voltage to a phase shifter in one arm of the silicon MZI modulator under test. Optical output from the modulator was input to a detection port of the network analyzer. There are two major factors that limit the EO response of the single silicon MZI modulators. One is RF loss in the phase shifter and the other is *RC* delay, as the roll-off frequency decreases with longer phase shifter length and stronger DC reverse bias voltage, respectively. A stronger DC reverse bias voltage leads to a lower PN-junction capacitance due to added expansion of the depletion region.

The roll-off frequency at 3-dB attenuation is as high as 33 GHz in the EO response of the silicon MZI modulator with 3-mm phase shifters. This allows a phase modulation in QPSK at 64 Gb/s and in DP-QPSK at 128-Gb/s, respectively. A longer phase shifter length is more preferable for optical modulation at lower symbol rates such as 10 Gbaud in OOK format with an advantage of a lower V_π. One can adjust the phase-shifter length according to requirements and specifications for the optical network under consideration.

16.3 Free-Carrier Plasma Dispersion for High-Speed Silicon Optical Modulator

16.3.1 Energy Transfer in Drude Theory

High-speed refractive-index modulation in silicon optical modulators is based on the free-carrier plasma dispersion, which is the real part of optical response of charged free carriers interacting with the optical field [16, 32–39]. The imaginary part of the optical response is free-carrier absorption, which has been extensively studied in semiconductors [40–52]. The kinetic energy and velocity of the charged free carriers are depicted schematically against time t in Fig. 16.8. The velocity increases linearly, while the kinetic energy increases quadratically with constant magnitude of the optical field. The optical response is suitable for optical modulators operating in a broad spectral range, such as the C and L bands, because the interaction is nonresonant and occurs irrespective of the wavelength of the incident optical field. Unbound individual carriers are involved in the interaction, and generate a negative refractive-index change with respect to an increase in carrier concentration, which is crucial for the elimination of frequency chirping as described below.

In case (a), where no scattering, or no dephasing, in other words, occurs, the charged carriers are accelerated coherently without disruption in the optical field and the energy of the optical field is transferred efficiently to the charged carriers. The optical-to-electronic energy transfer is inefficient, on the other hand, in case (b), where the charged carriers are not accelerated coherently due to dephasing in the carrier scattering. A large refractive-index change and a high optical absorption are
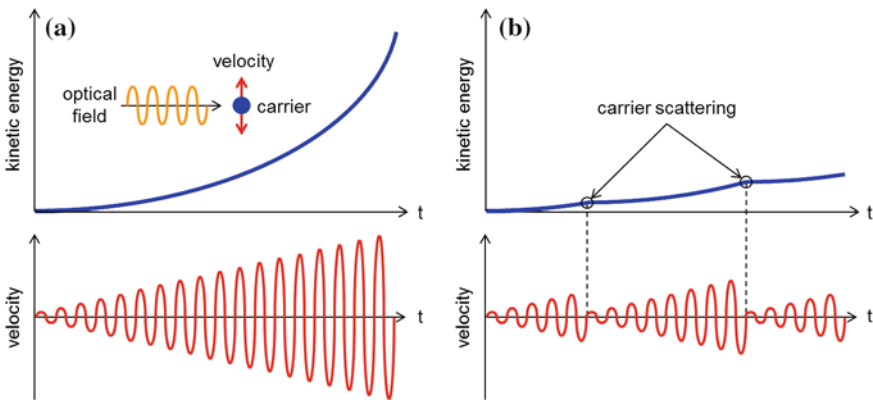

Fig. 16.8 Time evolution of the kinetic energy and velocity of charged free carriers interacting with the optical field in the case of carrier transport with no carrier scattering (**a**) and with carrier scattering (**b**)
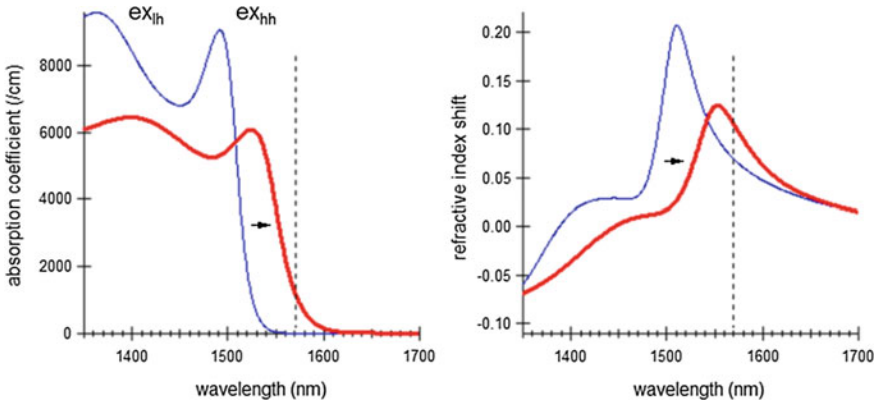
Fig. 16.9 Numerical optical absorption and refractive-index spectra for two-dimensional excitons in quantum well under zero bias (*thin curves*) and reverse bias (*thick curves*)

generated thereby if the charged carriers yield a high mobility according to the classical model of charged carrier transport [53]. Electronic band engineering for higher carrier mobility is an essential approach for a lower V_π in silicon-based optical modulators [54].

The refractive-index change in free-carrier plasma dispersion, Δn and optical loss change in free-carrier absorption, $\Delta\alpha$ are represented within the framework of Drude theory according to the following proportionalities [37]

$$\Delta n \propto -(N_e/m_e + N_h/m_h) \tag{16.3}$$

$$\Delta\alpha \propto -\left(N_e/m_e^2\mu_e + N_h/m_h^2\mu_e\right) \tag{16.4}$$

where, N_e, N_h, m_e, m_h, μ_e, and μ_h denote the electron concentration, hole concentration, electron effective mass, hole effective mass, electron mobility, and hole mobility, respectively. The key feature to note in these equations is that the refractive index change is negative for positive change in the optical loss. This characteristic is inherent to polarizability in the nonresonant optical response of free carriers [55] and crucial to zero-chirp modulation, as described in terms of frequency chirping below. In contrast, the refractive-index change in the quantum-confined Stark effect (QCSE) yields a positive change, which is opposite in sign to the free-carrier plasma dispersion, for a positive change in the optical loss in a wavelength region below the band edge of semiconductor quantum wells [17, 56] with optical absorption and refractive-index characteristics as schematically presented in Fig. 16.9. Model numerical spectra for the heavy-hole exciton (ex$_{hh}$) and light-hole exciton (ex$_{lh}$) in quantum wells were taken from the literature [57]. The QCSE is based on the resonant dipole transition of bound electron-hole states.

16.3.2   TEC-Free DC Optical Characteristics

The broadband nonresonant optical response of free carriers has the advantage of optical modulation in a wide temperature range without the need for a thermo-electric cooler (TEC). The change in silicon refractive index due to the thermo-optical effect [58] is not substantial and the optical phase drift induced by heat flow from adjacent active devices can be compensated by adjustment of the DC reverse bias voltage only. Evidence of TEC-free operation of a silicon optical modulator is presented as a DC bias voltage dependence of optical transmittance in Fig. 16.10. The device under test was a silicon single MZI modulator assembled on a chip carrier in a ceramic-based metal package, which is capable of 10-Gb/s OOK transmission in a 100-km link of single-mode fiber (SMF) at 25 °C [25]. Peak transmittance and dip wavelength were maintained between 20 and 80 °C with adjustment of the DC bias voltage applied to one of the MZI arms without a TEC. Therefore, the silicon optical modulator is a candidate for a small-footprint low-cost optical modulator operating in a TEC-free environment.

16.3.3   Frequency Chirping

Zero-chirp modulation is crucial for high-capacity signal transmission in optical transport networks with a high-spectral efficiency [18–21]. A MZI modulator is
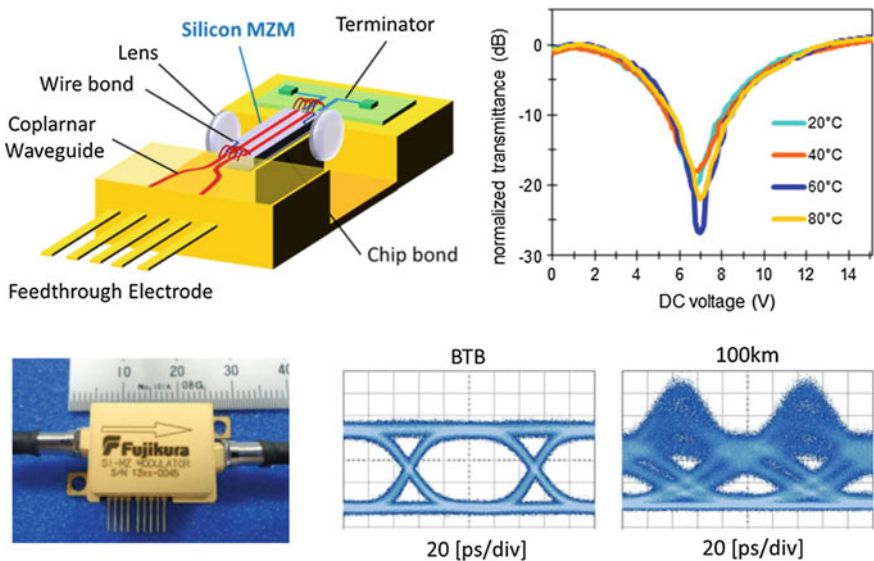

Fig. 16.10 Illustrated are a SI MZI modulator on a chip carrier, the DC bias voltage dependence of the normalized transmittance at temperatures between 20 and 80 °C, a modulator module assembled in a ceramic-based metal package, and 10-Gb/s eye diagrams in back-to-back (BTB) and in 100-km SMF transmission
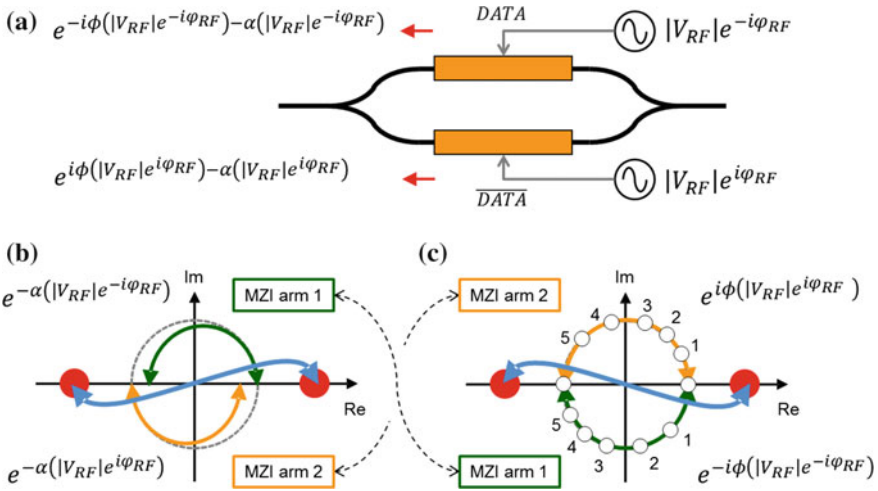
Fig. 16.11 **a** Configuration of RF signals and generated optical waves in each arm of the MZI in push-pull drive. **b** Schematic signal distortion due to the residual intensity modulation represented on a constellation diagram. **c** Schematic signal distortion due to the nonlinear bias dependence of the optical phase represented on a constellation diagram

capable of zero-chirp modulation in a wide spectral range extending over the C and L bands under push-pull drive [4, 13, 14]. It has been often argued that zero-chirp modulation may not be available for silicon optical modulators, because of the intensity modulation based on the free-carrier absorption as the counter part of refractive-index modulation based on the free-carrier plasma dispersion. However, this is not the case with silicon MZI modulators in which reverse-biased lateral PN-junction phase shifters are placed. Signal distortion due to the intensity modulation is compensated by the nonlinear voltage dependence of the phase shift, as illustrated in Fig. 16.11.

In push-pull operation, RF signals in opposite polarities are applied to the respective arms of the MZI, as depicted in Fig. 16.11a. Signal distortion due to the residual intensity modulation is indicated in the constellation diagram in Fig. 16.11b. The distortion is caused by the asymmetric intensity modulation between the two arms of the MZI. Another signal distortion in Fig. 16.11c is generated by the nonlinear voltage dependence of the optical phase shift, as shown in the experimental and numerical characteristics of the phase shift in Fig. 16.4. The latter signal distortion, which is 180° reversed against the distortion due to the residual intensity modulation, cancels with the former signal distortion. Quasi-zero-chirp modulation is thus possible for a silicon MZI modulator with reverse-biased lateral PN junction phase shifters. The inversion of the signal distortion is a consequence of the negative sign in (16.3), inherent to the nonresonant optical response of free carriers in semiconductors over a broad spectral range.
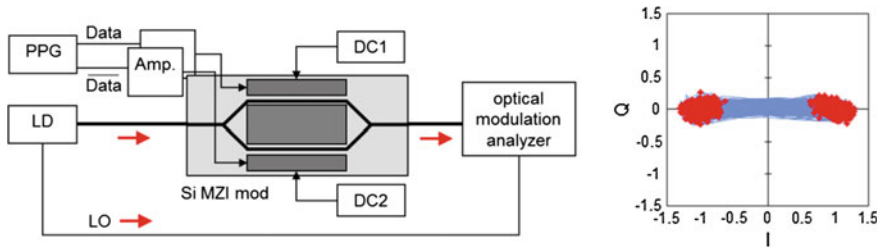
Fig. 16.12 Measurement block diagram and constellation diagram for 22.3 Gb/s BPSK in back-to-back characterization

Quasi-zero-chirp modulation has been confirmed for 22.3-Gb/s BPSK modulation, as presented in Fig. 16.12. The constellation was measured for a back-to-back BPSK signal for confirmation of zero-chirp modulation. In the constellation measurement, the optical signal output from a Si single MZI modulator was input to 90° optical hybrid circuit for coherent homodyne detection and transients of in-phase (I) and quadrature (Q) electric signals were acquired by a real-time oscilloscope. In the BPSK constellation diagram, trajectories in bit transmission are laid along the real axis with residual chirp $|\alpha| < 0.1$. Zero ($x = 1$) and π ($x = -1$) bits are indicated as red points and trajectories of transition between the two bits are in light blue. The trajectories are linear and located on the real axis (x axis) with no imaginary part ($y = 0$).

16.4   Silicon Optical Modulators in High-Capacity Optical Networks

16.4.1   On-off Keying Characteristics

Extensive efforts have been devoted to silicon OOK modulators [59–62]. High-speed OOK modulation has been achieved using a push-pull silicon MZI modulator with reverse-biased lateral PN-junction phase shifters and back-to-back performances have been reported with an extinction ratio of 3.8 dB at 60 Gb/s [62]. High-contrast OOK modulation with an extinction ratio beyond 10 dB was reported and the bit error rate (BER) was characterized for a push-pull silicon single MZI modulator at 11.1 Gb/s [14].

In BER measurements using a BER tester (BERT), different lengths of SMF (20, 40, 60, and 80 km) with a positive dispersion parameter of 17 ps/nm/km at 1550 nm were used. BER measurements were also performed for a negative dispersion parameter using dispersion compensation fiber modules (DCFMs) designed for dispersion compensation for 20, 40, 60, and 80-km SMFs, respectively. The modulation format applied was a 11.1-Gbps nonreturn-to-zero OOK (NRZ-OOK) and pseudo-random bit stream (PRBS) in a bit length of $2^{31}-1$ from a pulse-pattern generator (PPG). To avoid BER degradation due to a fluctuation in clock timing, a
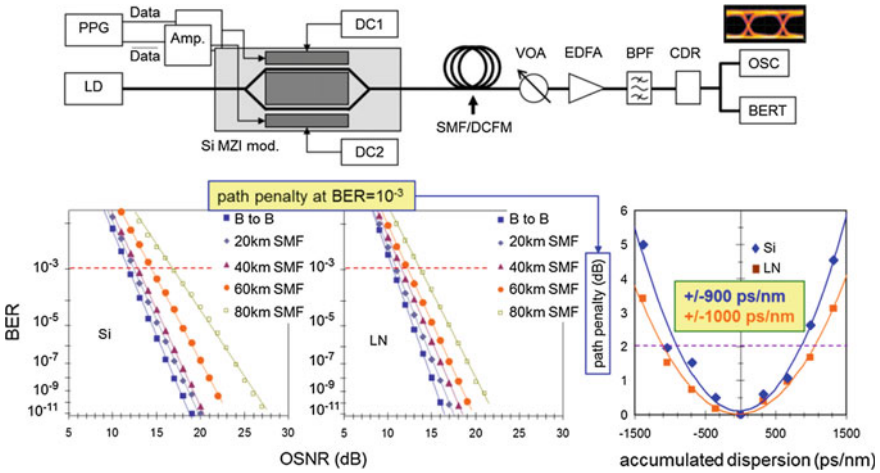
Fig. 16.13 Measurement block diagram for transmission experiments in zero-chirp modulation (*upper*) and characteristics of BER and dispersion tolerance in comparison with a LN modulator (*lower*)

clock data recovery (CDR) unit was incorporated to the receiver unit. The wavelength from a single-mode laser source (LD) was 1550 nm. For BER measurements with variable OSNR, the noise source was amplified spontaneous emission (ASE) in an Er-doped fiber amplifier (EDFA). Control of OSNR was provided by variable attenuation of the transmitted optical signals at a variable optical attenuator (VOA). The bandwidth of ASE was limited by an optical bandpass filter (BPF) within 1-nm full bandwidth at 3-dB attenuation. The OSNR was independently measured by an optical spectrum analyzer with 0.1-nm resolution bandwidth for the noise component as used in other transmission experiments [63]. Eye diagrams were acquired using a sampling oscilloscope (OSC) instead of BERT.

The BER characteristics for the Si MZI modulator and a LN single MZI modulator are plotted in Fig. 16.13. The Si MZI modulator yields a BER performance similar to the LN MZI modulator. The dispersion penalty at a BER of 10^{-3} is also plotted for both MZI modulators in Fig. 16.13.

The accumulated dispersion in the horizontal axis corresponds to the accumulated chromatic dispersion in the respective fiber lengths for SMFs or DCFMs. The dispersion penalty of the Si MZM is very close to that of the LN MZI modulator and almost symmetric with respect to the minimum at zero dispersion (back to back). The zero-chirp modulation in the Si MZI modulator is thus confirmed also in the characteristics of the dispersion penalty. The dispersion penalty of the Si MZI modulator is approximately 2-dB higher at 1320 ps/nm/km (80-km SMF) in comparison with that of the LN MZI modulator. It can be eliminated with further enhancement of high-speed performance of the Si MZI modulator by more precise adjustment of the impedance matching of the traveling-wave electrodes and high-conductivity metallization in the RF regime [64].

16.4.2   *Phase-Shift Keying Characteristics*

16.4.2.1   **Bpsk**

The transmission performance of the Si single MZI modulator was evaluated in BPSK at a bit rate of 22.3 Gb/s (11.1-Gbaud symbol rate). The Si MZI modulator was driven in push-pull mode at 8-Vpp amplitude. The actual bitrate of 22.3 Gb/s was intended for 20-Gb/s transmission with accommodation of forward error correction. Eye diagrams and BER measurements were performed in direct differential detection using a 1-bit delay line interferometer (DLI) connected to a balanced photodetector (PD), as depicted in Fig. 16.14. The two types of transmission fibers were used as in the OOK measurements: SMFs for distances up to 20 km and DCFMs, allowing BER measurements with positive and negative accumulated dispersion ranging from –347 to +334 ps/nm. The electrical signal output from the balanced PD was detected with BERT. In eye-diagram measurements, a sampling oscilloscope was connected to the balanced PD instead of the BERT.

Eye diagrams of the BPSK signals with positive and negative accumulated dispersion after transmission through the SMFs and DCFMs are presented in comparison with the back-to-back eye diagram in Fig. 16.14. The eye opening is closed and the signal waveform is more distorted on account of a more highly accumulated dispersion with increasing transmission distance. Eye diagrams with almost the same magnitude of accumulated dispersion are similar each other due to zero chirping in the optical signal generated in the Si MZI modulator.
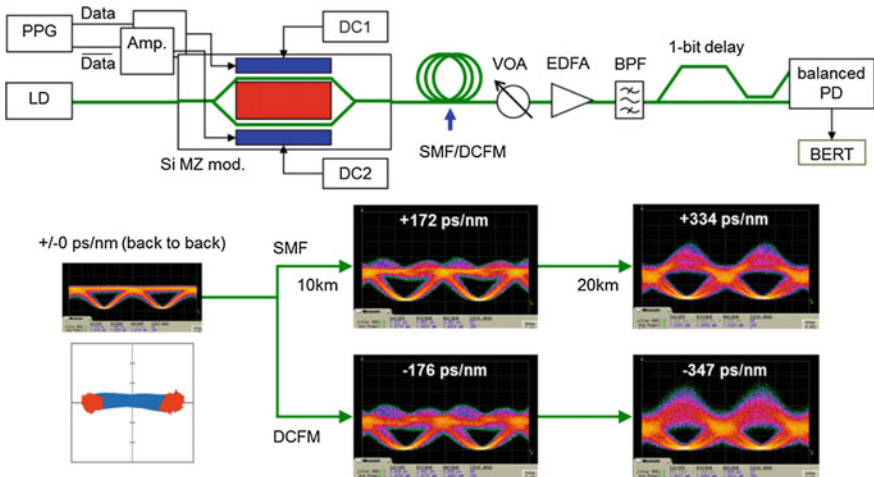

Fig. 16.14 Measurement block diagram for differential detection in BPSK (*upper*) and transmission eye diagrams (*lower*)
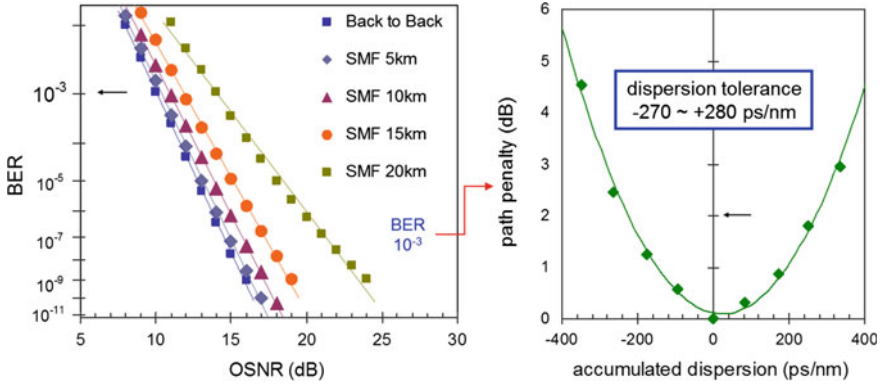
Fig. 16.15 BER characteristics in SMF transmission up to 20 km and the dispersion tolerance obtained from path penalty characteristics

BER characteristics are plotted in Fig. 16.15 as a function of OSNR for transmission through the SMFs. The BER has been measured also for transmission through the DCFMs. The path penalty is obtained as an OSNR penalty in the fiber transmission at BER = 10^{-3} (indicated with an arrow). Path penalty is plotted against accumulated dispersion in Fig. 16.15. The points in the positive side of accumulated dispersion are obtained for transmission through the SMFs, and those in the negative side for transmission through the DCFMs. The solid curve is a fitting curve using a quadratic dependence on accumulated dispersion. The path penalty is symmetric around zero accumulated dispersion, implying zero-chirp modulation. The accumulated dispersion for 2-dB path penalty is –220 and +230 ps/nm. From these values, the dispersion tolerance is 550 ps/nm with 13-dB OSNR. The Si MZI modulator can be used as a small-footprint modulator for 20-Gb/s data transmission in BPSK.

16.4.2.2   Qpsk

Figure 16.16 shows the top-view photograph of a silicon IQ modulator chip for QPSK, which was fabricated on an 8-inch SOI wafer using CMOS compatible processes. The modulator consists of a nested IQ MZI. The nested IQ MZI has two sub-MZIs for I and Q components, respectively, including the rib-waveguide lateral PN-junction phase shifters connected to straight coplanar-waveguide electrodes. The electrodes are connected to input and output contact pads at the edge of the modulator chip with a minimum length without bend waveguides. This design minimizes RF propagation loss on a silicon wafer. A thermo-optic (TO) DC phase shifter allows phase adjustment to sustain a $\pi/2$ phase difference between I and Q sub-MZIs for stable QPSK modulation. These device blocks were monolithically integrated in a footprint as small as 3.5×2.9 mm^2. Phase shift and optical loss of the silicon rib-waveguide phase shifter with a 3-mm length were measured using a test sample
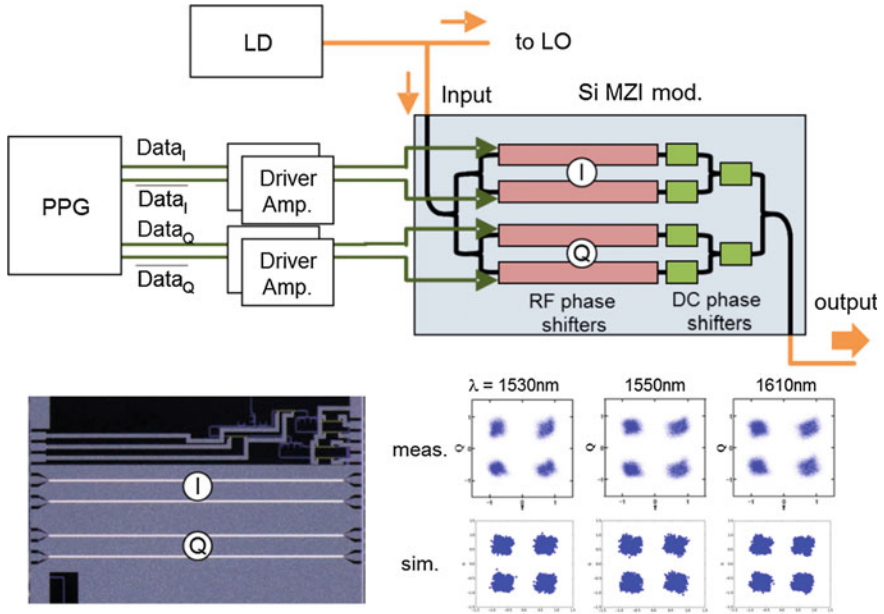
Fig. 16.16 Layout of silicon QPSK modulator chip and measurement block diagram (*upper*) and *top-view* photograph of a small-footprint monolithic QPSK chip with measured and simulated constellation diagrams (*lower*)

of an asymmetric silicon MZI waveguide. V_π is 7.5 V and the optical loss is as low as 2.7 dB at zero bias voltage and 1.9 dB at 5-V reverse-bias voltage, respectively.

The output laser beam from the LD was split into two paths: input light to the modulator and local oscillator (LO) light for homodyne coherent detection in the optical modulation analyzer. Measured and simulated QPSK constellation diagrams of the silicon IQ MZI modulator at 64 Gb/s (32-Gbaud symbol rate) at wavelengths of 1530, 1550, and 1610 nm are plotted in Fig. 16.16. Bit spots are clearly resolved in the measured constellation diagrams. Therefore, 64-Gb/s QPSK modulation is confirmed for the Si IQ MZI modulator. The advantage of a powerful 3rd-generation forward error correction (FEC) in 50-Gb/s QPSK transmission [65] can be accommodated in a capacity of the full transmission rate as high as 64 Gb/s.

Good agreement of the simulated constellation diagrams with the measured diagrams was obtained [66]. Silicon optical modulators for QPSK application can be designed and fabricated on the basis of the silicon photonic platforms for design and fabrication.

16.4.2.3 Dp-Qpsk

A silicon MZI modulator designed for 128-Gb/s DP-QPSK application at 32-Gbaud, in which 3-mm silicon rib-waveguide lateral PN-junction phase shifters
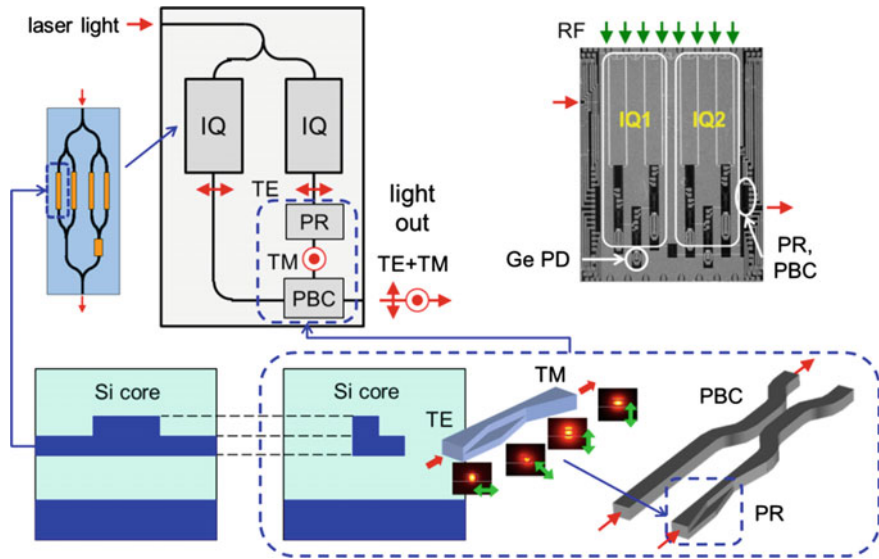
Fig. 16.17 Layout and *top-view* photograph of an ultrasmall-footprint monolithic silicon PDM IQ modulator with the illustrated PDM optical circuit

for IQ modulation were disposed in each arm of IQ MZIs, was fabricated as shown in Fig. 16.17. The Si MZI modulator consists of two IQ MZI modulator units and a waveguide circuit for polarization-division multiplexing (PDM).

A silicon PDM IQ MZI modulator consists of the following four blocks: (16.1) an input waveguide split into two parallel waveguides with a multi-mode interferometer, (16.2) two IQ MZI modulators, each of which consists of a silicon nested MZI incorporating silicon single sub-MZIs on both parent MZI arms and operating in TE polarization, (16.3) a polarization rotator (PR), with which the polarization of the light after one of the IQ MZMs is converted to transverse-magnetic (TM) polarization and (16.4) a polarization beam combiner (PBC) to multiplex TE and TM polarization outputs [67, 68]. A Si PDM IQ MZM was monolithically integrated in an ultrasmall footprint of 6.5×5 mm^2 with Ge PDs for performance monitoring and Si rib-waveguide TO DC phase shifters to the adjust phase difference to $\pi/2$ between I and Q components in each polarization. The rib-waveguide-based PR in PDM circuit was designed with common design rules for the rib-waveguide phase shifter, thereby being suitable for high-yield low-cost fabrication.

A Si PDM IQ MZM was mounted in a ceramic-based metal package with four modulator drivers in dimensions of $35 \times 15 \times 4.5$ mm^3, as shown in Fig. 16.18 [69]. Butt fiber coupling with 2.5-dB coupling loss, 1-dB polarization-dependent loss, and 40-dB return loss was achieved for low-profile packaging by using suspended MFCs [70]. The optical insertion loss was measured to be lower than 15 dB in the C band. The output single-ended signal of 0.5 Vpp was directly applied to the
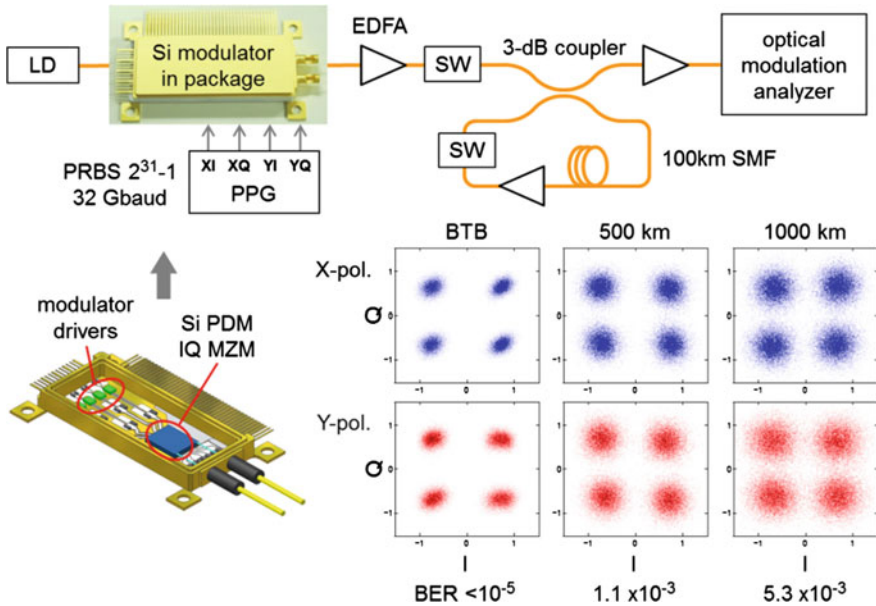
Fig. 16.18 Block diagram of the 128-Gb/s digital coherent transmission experiment based on a 100-km SMF loop link (*upper*), perspective illustration of the silicon DP-QPSK modulator module, and constellation diagrams in X and Y polarization states in transmission up to 1000-km SMF

modulator module and it was amplified to ±3.25 V in a low-power driver amplifier in the module. The LD output was 14 dBm at a wavelength of 1540 nm. A further reduction in the drive voltage will be achieved by design refinement of the rib-waveguide phase shifters for a reduction in power consumption.

Long-haul transmission measurements were performed using a 100-km SMF loop link [69]. Two optical switches (SWs) allowed synchronized burst-mode loop transmission in 50 and 100 loop turns to reach 500 and 1000-km total spans, respectively. The transmitted optical signals were detected with a coherent receiver and demodulated with an offline digital signal processor (DSP) to obtain constellation diagrams in the two orthogonal linear polarization states [19, 20].

As another example of a monolithic silicon modulator for digital coherent communication has been reported [71]; a 112-Gb/s DP-QPSK using a monolithic Si PDM IQ modulator, in which a strip-loaded Si waveguide as a PR was integrated with Si MZI IQ modulators. A silicon-nitride tapered strip was loaded on the Si core of the PR with a SiO_2 spacer layer between the Si_3N_4 strip and the Si core. An integrated small-footprint transceiver using a monolithic silicon PDM IQ modulator in a CFP package was reported [72]. Monolithic silicon optical modulators continue to progress for applications to high-capacity optical networks in various modulation formats.

16.5   Conclusion

Monolithically integrated silicon optical modulators are reviewed in the light of small-footprint high-speed optical modulators operating in various modulation formats in high-capacity optical networks. Free carriers interacting with the optical field allow the optical modulation to be insensitive to the ambient temperature, and thereby TEC-free operation is expected for the small-footprint low-cost optical modulators designed and fabricated on a silicon photonics platform. The nonresonant optical response of free carriers has the advantage of zero-chirp modulation in a push-pull drive toward high-speed optical transmission with high-spectral efficiency. Low-profile compact packaging technology has been developed concurrently with the progress of silicon modulator chips. The integrated silicon optical modulators are suitable for small-footprint optical transceivers in energy-efficient high-capacity optical networks.

References

1. K. Kawano, High-speed Ti:LiNbO$_3$ and semiconductor optical modulators. IEICE Trans. Electron. **E76-C**, 183–190 (1993)
2. E.L. Wooten, K.M. Kissa, A. Yi-Yan, E.J. Murphy, D.A. Lafaw, P.F. Hallemeier, D. Maack, D.V. Attanasio, D.J. Fritz, G.J. McBrien, D.E. Bossi, A review of lithium niobate modulators for fiber-optic communications systems. IEEE J. Sel. Top. Quantum Electron. **6**, 69–82 (2000)
3. L. Thylén, U. Westergren, P. Holmström, R. Schatz, P. Jänes, Recent developments in high-speed optical modulators, in *Optical fiber telecommunications V A components and subsystems* (Academic, San Diego, 2008) (Chap. 7)
4. A.H. Gnauck, P.J. Winzer, Optical phase-shift-keyed transmission. J. Lightwave Technol. **23**, 115–130 (2005)
5. K.-P. Ho, *Phase-Modulated Optical Communication Systems* (Springer, New York, 2005)
6. W.S.C. Chang, *RF Photonic Technology in Optical Fiber Links* (Cambridge, New York, 2002)
7. I.A. Young, E. Mohammed, J.T.S. Liao, A.M. Kern, S. Palermo, B.A. Block, M.R. Reshotko, P.L. Chang, Optical I/O technology for tera-scale computing. IEEE Com. Mag. **48**(10), 184–191 (2010)
8. Y.A. Vlasov, Silicon CMOS-integrated nano-photonics for computer and data communications beyond 100G. IEEE Com. Mag. **50**(2), S67–S72 (2012)
9. Y. Arakawa, T. Nakamura, Silicon photonics for next generation system integration platform. IEEE Com. Mag. **51**(3), 72–77 (2013)
10. T. Baehr-Jones, T. Pinguet, P. Lo G.-Q., S. Danziger, D. Prather, M. Hochberg, Myths and rumours of silicon photonics. Nat. Photon. **6**, 206–208 (2012)
11. Workshop: Silicon photonics: Is it still in hype or on its way to the field?, Symposium: Beyond the gold box: the future of integrated optics I-III, in *Optical Fiber Communication Conference and Exposition (OFC)*, (OSA, Washington, DC, 2015) S1A, W1H-W3H
12. K. Goi, A. Oka, H. Kusaka, Y. Terada, K. Ogawa, T.-Y. Liow, X. Tu, G.-Q. Lo, D.-L. Kwong, Low-loss high-speed silicon IQ modulator for QPSK/DQPSK in C and L bands. Opt. Express **22**, 10703–10709 (2014)
13. F. Koyama, K. Iga, Frequency chirping in external modulators. J. Lightwave Technol. **6**, 87–93 (1988)

14. K. Goi, K. Oda, H. Kusaka, Y. Terada, K. Ogawa, T.-Y. Liow, X. Tu, G.-Q. Lo, D.-L. Kwong, 11-Gb/s 80-km transmission performance of zero-chirp silicon Mach-Zehnder modulator. Opt. Express **20**, B350–B356 (2012)

15. K. Ogawa, K. Goi, Y.T. Tan, T.-Y. Liow, X. Tu, Q. Fang, G.-Q. Lo, D.-L. Kwong, Silicon Mach-Zehnder modulator of extinction ratio beyond 10 dB at 10.0–12.5 Gbps. Opt. Express **19**, B26–B31 (2011)

16. R.A. Soref, B. A. Bennett, Electrooptical effects in silicon. IEEE J. Quantum Electron. **QE-23**, 123–129 (1987)

17. D.A.B. Miller, J.S. Weiner, D.S. Chemla, Electric-field dependence of linear optical properties in semiconductor quantum well structures: waveguide elecroabsorption and sum rules. IEEE J. Quantum Electron. **QE-22**, 1816–1830 (1986)

18. P.J. Winzer, R.-J. Essiambre, Advanced optical modulation formats. Proc. IEEE **94**, 952–985 (2006)

19. K. Kikuchi, Coherent transmission systems, in *34th European Conference and Exhibition on Optical Communication* (ECOC2008, 21–25 September 2008, Brussels, Belgium) Th.2.A.1

20. K. Kikuchi, Coherent optical communication systems, in *Optical Fiber Telecommunications V B Systems and Networks* (Academic, San Diego, 2008) (Chap. 3)

21. G.P. Agrawal, *Fiber-optic Communication Systems*, 4th edn. (Wiley, Hoboken, 2010)

22. T.-Y. Liow, K.-W. Ang, Q. Fang, J.-F. Song, Y.-Z. Xiong, M.-B. Yu, Guo-Qiang Lo, D.-L. Kwong, Silicon modulators and germanium photodetectors on SOI: monolithic integration, compatibility, and performance optimization. IEEE J. Sel. Top. Quantum Electron. **16**, 307–315 (2010)

23. F.Y. Gardes, G.T. Reed, N.G. Emerson, C.E. Png, A sub-micron depletion-type photonicmodulator in silicon on insulator. Opt. Express **13**, 8845–8854 (2005)

24. B. Analui, D. Guckenberger, D. Kucharski, A. Narasimha, A fully integrated 20-Gb/s optoelectronic transceiver implemented in a standard 0.13-μm CMOS SOI technology. IEEE J. Solid-State Circ. **41**, 2945–2955 (2006)

25. K. Ogawa, H. Ishihara, K. Goi, Y. Mashiko, S.T. Lim, M.J. Sun, S. Seah, C.E. Png, T.-Y. Liow, X. Tu, G.-Q. Lo, D.-L. Kwong, Fundamental characteristics and high-speed applications of carrier-depletion silicon Mach-Zehnder modulators. IEICE Electron. Express **11**, 20142010 (2014)

26. H. Kusaka, A. Oka, K. Goi, K. Ogawa, T.-Y. Liow, X. Tu, G.-Q. Lo, D.-L. Kwong, Monolithic photonic integrated circuit for optical performance monitoring of silicon Mach-Zehnder modulator in C and L bands, in *18th OptoElectronics and Communications Conference (OECC)* (30 June–4 July 2013, Kyoto) MM1-4

27. K. Ogawa, K. Goi, H. Kusaka, Y. Terada, T.-Y. Liow, X. Tu, G.-Q. Lo, D.-L. Kwong, V. Dixit, S. T. Lim, C. E. Png, Low-loss high-speed silicon Mach-Zehnder modulator for optical-fiber telecommunications. Proc. SPIE **8629**, 86290U-1-86290U-8 (2013)

28. Fimmwave, http://www.photond.com/products/fimmwave.htm

29. C.E. Png, V. Dixit, S.T. Lim, E.-P. Li, Accurate high-speed eye diagram simulation of silicon-based modulators. Proc. SPIE **8629**, 86290S-1 (2013)

30. C.E. Png, S.P. Chan, S.T. Lim, G.T. Reed, Optical phase modulators for MHz and GHz modulation in silicon-on-insulator (SOI). J. Lightwave Technol. **22**, 1573–1581 (2004)

31. X. Tu, T.-Y. Liow, J. Song, M.B. Yu, G.-Q. Lo, Fabrication of low loss and high speed silicon optical modulator using doping compensation method. Opt. Express **19**, 18029–18035 (2011)

32. W.L. Bond, B.G. Cohen, R.C.C. Leite, A. Yariv, Observation of the dielectric-waveguide mode of light propagation in p-n junctions. Appl. Phys. Lett. **2**, 57–59 (1963)

33. A.K. Jonscher, M.H. Boyle, The flow of carriers and its effect on the spatial distribution of radiation from injection lasers. Proc. Symp. GaAs **12A** (1966)

34. G.H.B. Thompson, A theory for filamentation in semiconductor lasers including the dependence of dielectric constant on injected carrier density. Opt. Quantum Electron. **4**, 257–310 (1972)

35. O. Mikami, H. Nakagome, Waveguide optical switch in InGaAs/InP using free-carrier plasma dispersion. Electron. Lett. **20**, 228–229 (1984)

36. M. Asada, Theoretical linewidth enhancement factor α of GaInAs/InP lasers. IEICE Trans. **E68**, 518–520 (1985)
37. R.A. Soref, J.P. Lorenzo, All-silicon active and passive guided-wave components for λ = 1.3 and 1.6 μm. IEEE J. Quantum Electron. **22**, 873–879 (1986)
38. R.A. Soref, J.P. Lorenzo, Silicon guided-wave optics. Solid State Technol. **31**(11), 95–98 (1988)
39. B.R. Bennett, R.A. Soref, J.A. Del Alamo, Carrier-induced change in refractive index of InP, GaAs, and InGaAsP. IEEE J. Quantum Electron. **26**, 113–122 (1990)
40. M. Becker, H.Y. Fan, Optical properties of semiconductors. II. Infra-red transmission of germanium. Phys. Rev. **76**, 1530–1531 (1949)
41. M. Becker, H.Y. Fan, Optical properties of semiconductors. III. Infra-red transmission of silicon. Phys. Rev. **76**, 1531–1532 (1949)
42. H.B. Briggs, Infra-red absorption in silicon. Phys. Rev. **77**, 727–722 (1950)
43. H.B. Briggs, R.C. Flecher, Absorption of infrared light by free carriers in germanium. Phys. Rev. **91**, 1342–1346 (1953)
44. H.Y. Fan, W. Spitzer, J.R. Collins, Infrared absorption.in n-type germanium. Phys. Rev. **101**, 566–572 (1956)
45. W. Spitzer, H.Y. Fan, Infrared absorption in n-type silicon. Phys. Rev. **108**, 268–271 (1957)
46. R. Rosenberg, M. Lax, Free-carrier absorption in n-type Ge. Phys. Rev. **112**, 843–852 (1958)
47. W.G. Spitzer, J.M. Whelan, Infrared absorption and electron effective mass in n-type ga1lium arsenide. Phys. Rev. **114**, 59–63 (1959)
48. H.R. Riedl, Free-carrier absorption in PbTe. Phys. Rev. **127**, 162–166 (1962)
49. R.M. Culpepper, J.R. Dixon, Free-carrier absorption in n-type indium arsenide. J. Opt. Soc. Am. **58**, 96–102 (1968)
50. J.D. Wiley, M. Didomenico, Free-carrier absorption in n-type GaP. Phys. Rev. B **1**, 1655–1659 (1970)
51. A.H. Kahn, Theory of the infrared absorption of carriers in germanium and silicon. Phys. Rev. **97**, 1647–1652 (1955)
52. W.P. Dumke, Quantum theory of free carrier absorption. Phys. Rev. **124**, 1813–1817 (1961)
53. P. Drude, Zur elektronentheorie der metalle. Ann. der Physik **306**, 566–613 (1900)
54. M. Takenaka, S. Takagi, Strain engineering of plasma dispersion effect for SiGe optical modulators. IEEE J. Quantum Electron. **48**, 8–16 (2012)
55. R.W. Boyd, *Nonlinear Optics*, 3rd ed. (Academic, San Diego, 2008) (Chap. 13)
56. X.B. Mei, K.K. Loi, H.H. Wieder, W.S.C. Chang, C.W. Tu, Strain-compensated InAsP/GaInP multiple quantum wells for l.3 μm waveguide modulators. Appl. Phys. Lett. **68**, 90–92 (1996)
57. K. Ogawa, Y. Matsui, Time-frequency spectroscopy of an InGaAs/InP quantum-well exciton Bragg reflector. Appl. Phys. Lett. **74**, 2569–2571 (1999)
58. H.Y. Fan, Temperature dependence of the energy gap in semiconductors. Phys. Rev. **82**, 900–905 (1951)
59. L. Liao, A. Liu, D. Rubin, J. Basak, Y. Chetrit, H. Nguyen, R. Cohen, N. Izhaky, M. Paniccia, 40 Gbit/s silicon optical modulator for high-speed applications. Electron. Lett. **43**, 1196–1197 (2007)
60. D.J. Thomson, F.Y. Gardes, Y. Hu, G. Mashanovich, M. Fournier, P. Grosse, J.-M. Fedeli, G.T. Reed, High contrast 40Gbit/s optical modulation in silicon. Opt. Express **19**, 11507–11516 (2011)
61. P. Dong, L. Chen, Y.-K. Chen, High-speed low-voltage single-drive push-pull silicon Mach-Zehnder modulators. Opt. Express **20**, 6163–6169 (2012)
62. D. Patel, S. Ghosh, M. Chagnon, A. Samani, V. Veerasubramanian, M. Osman, D.V. Plant, Design, analysis, and transmission system performance of a 41 GHz silicon photonic modulator. Opt. Express **23**, 14263–14287 (2015)
63. T. Mizuochi, K. Ishida, T. Kobayashi, J. Abe, K. Kinjo, K. Motoshima, K. Kasahara, A comparative study of DPSK and OOK WDM transmission over transoceanic distances and their performance degradations due to nonlinear phase noise. J. Lightwave Technol. **21**, 1933–1943 (2003)

64. Y. Yang, Q. Fang, M. Yu, X. Tu, R. Rusli, G.-Q. Lo, High-efficiency Si optical modulator using Cu travelling-wave electrode. Opt. Express. **22**, 29978 (2014)
65. Y. Miyata, W. Matsumoto, K. Onohara, T. Sugihara, K. Kubo, A triple-concatenated FEC using soft-decision decoding for 100 Gb/s optical transmission, in *Optical Fiber Communication Conference and Exposition* (Optical Society of America, San Diego, 2010) OThL3
66. C.E. Png, M.J. Sun, S.T. Lim, K. Ogawa, Accurate modelling and simulation of silicon optical modulators in QPSK. Proc. SPIE **9367**, 93670F (2015)
67. K. Goi, H. Kusaka, A. Oka, K. Ogawa, T.-Y. Liow, X. Tu, G.-Q. Lo, D.-L. Kwong, OFC digest **W1I**, 2 (2014)
68. K. Goi, A. Oka, H. Kusaka, K. Ogawa, T.-Y. Liow, X. Tu, G.-Q. Lo, D.-L. Kwong, Low-loss partial rib polarization rotator consisting only of silicon core and silica cladding. Opt. Lett. **40**, 1410–1413 (2015)
69. K. Goi, K. Oda, H. Ishihara, R. Matsumoto, Y. Mashiko, K. Ogawa, T.-Y. Liow, X. Tu, G.-Q. Lo, D.-L. Kwong, 128 Gb/s DP-QPSK silicon modulator module integrated with driver amplifiers, ECOC digest (2014) P.2.20
70. Q. Fang, T.-Y. Liow, J.F. Song, C.W. Tan, M.B. Yu, G.Q. Lo, D.-L. Kwong, Opt. Exp. **18**, 7763 (2010)
71. P. Dong, C. Xie, L. Chen, L.L. Buhl, Y.-K. Chen, 112-Gb/s monolithic PDM-QPSK modulator in silicon. Opt. Express **20**, B624–B629 (2012)
72. C. Doerr et al., Single-Chip Silicon Photonics 100-Gb/s Coherent Transceiver, Proceedings of OFC, Th5C.1, San Francisco (2014)